JOURNAL OF MATERIALS SCIENCE 32 (1997) 5035–5045

Fracturing of industrial diamond plates

K. L. JACKSON, D. L. THURSTON, P. J. BOUDREAUX
Laboratory for Physical Sciences, College Park, MD 20740, USA

R. W. ARMSTRONG
University of Maryland, College Park, MD 20742, USA

C. CM. WU
Naval Research Laboratory, Washington, DC 20375, USA

Indentation hardness and three-point bend tests were performed on perforated synthetic diamond substrates designed for use in a three-dimensional cube computer architecture based on interconnected stacking of multichip modules. The fracture strengths in bending of two substrate materials, with and without laser drilled interconnect ''via holes'', were correlated with optical and scanning electron microscope (SEM) observations of the fracture surfaces, thus providing for matching of fracture strengths with different growth microstructures within the plates and, also, with the extent of weakening produced by the via holes. The relatively high strength levels, characteristic of diamond material, were found to be lowered somewhat either by a filamentary pattern of growth fissures in one material or less so by apparent cleavage fracturing among textured grains in a second material. In the latter case, the technique of fracture surface topography analysis (FRASTA) provided evidence of plastic flow having occurred during fracturing.

1. Introduction

Recent accomplishments in synthetic diamond technology have led to the development of an advanced three-dimensional cube computer employing diamond based multichip modules (MCMs) [1, 2]. The extraordinary thermal conductivity, dielectric properties and strength of diamond are important characteristics associated with the design of thin polycrystalline diamond substrates for the individual MCMs. Fig. 1 illustrates a current system design for effective thermal management and heat removal. Silicon chips are mounted to a 1 mm thick diamond plate and a high density interconnect of copper and polyimide is applied to form each MCM. Improved thermal performance is obtained against similar MCMs that use ceramic substrates. A 10 cm cube architecture was envisioned to decrease both the size and cycle time of present supercomputing devices, in order to achieve subnanosecond performance. The diamond based MCMs (measuring roughly $10 \times 10\ \text{cm} \times 1\ \text{mm}$) are stacked with vertical interconnects to the MCMs, above and below, by way of numerous laser drilled and metal filled "via holes" in each substrate. The via patterns were presumed to have a detrimental effect on the fracture strength of the plates and there were questions, too, of added damage to the diamond material accruing in the thermomechanical drilling process. The correlation of strength properties with growth structure was of additional interest. Consequently, diamond material was obtained from two suppliers whose products, designated here as material A or B, were visibly different and exhibited different thermal conductivities: 13.2 W $\text{cm}^{-1}\,\text{K}$ for material A and 10.0–12.0 W $\text{cm}^{-1}\,\text{K}$ for material B.

2. Experimental procedure

2.1. Microstructure of the material

Polycrystal grain sizes, surface crack-like grooves between clustered grains, penetrating fissures along particular grain boundaries and entrapped porosity were microstructural features of concern. The polycrystal grain size is recognized by changes of reflectivity in side views of beam specimens, shown in Fig. 2 for both diamond materials. The side surfaces of the beam specimens result from laser beam cutting through the 1.0 mm plate thickness. Along the nucleation surface (bottom edge) where diamond growth initiated, say, in material B, the polycrystal grain size is smaller, on the order of 0.01 mm in width, while along the growth surface (top edge) where the crystals have grown to larger size for certain grain orientations, the polycrystal grain size is definitely larger, on the order of 0.04 ± 0.01 mm. Thus a ratio of 4 : 1 appears to apply for the comparison of grain widths between growth and nucleation surfaces, respectively. By comparison, material A appears to have a somewhat smaller grain size on the nucleation surface, but a larger grain size from exaggerated widening of certain grains in reaching the growth surface. A largest grain size of 0.2 mm was recognizable on the growth surface of material A. The difference in polycrystal grain widths between the two surfaces also results in recognizable differences

0022–2461

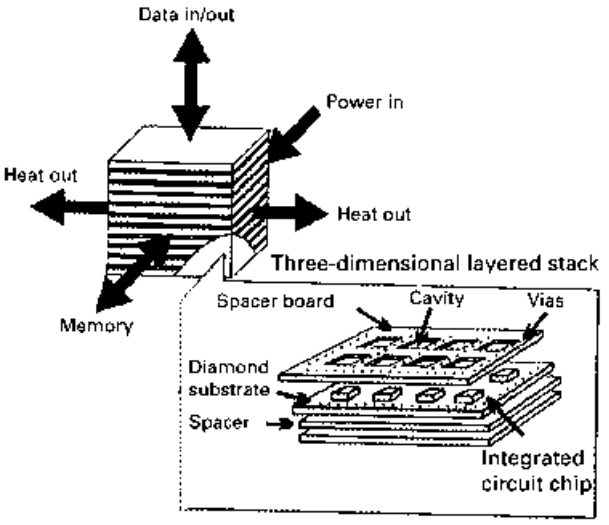

Figure 1 Vertically stacked and interconnected, diamond based multichip modules form a cube shape and the basis for an advanced three-dimensional architecture (has 20 kW heat removal capacity over 1.048 cm^3).

between the macroscopic surface appearances. Fig. 3 shows the smoother nucleation and rougher growth surfaces of a material A beam specimen.

Surface crack networks on the polished growth surfaces of material A specimens gave an indication of a filamentary crack structure penetrating into the plate material. The networks of surface cracks appear to result from the anisotropic growth of individual or clumped crystals, thus occurring along boundaries between the grains. Entrapped porosity was also a concern because of the diamond crystals impinging on one another during competition for growth in various directions, possibly producing internally trapped voids within the material and degrading the strength of the material.

The potential influence of the laser drilled via holes was of major concern in the consideration of the material strength degradation to the diamond plates. A typical via hole drilled into a material A beam sample is shown in Fig. 4 at both the plate entry and exit surfaces. In this case, the holes were uniformly drilled following the use specification of 102 μm diameter. At the entrance (growth) surface, the hole is nearly round, while upon exit, the hole is slightly larger and irregularly shaped. Although there was concern about possible radial cracks emanating from the holes as a result of thermal stresses in the drilling process, none were observed. Additionally, there was concern over the subsequent influence of stress concentrations from the holes. The entry view in Fig. 4 also shows the surface crack network mentioned previously.

Both material A and B diamond specimens were closely examined through optical microscopy and a photographic record was kept. The photographs seen in Figs 2–4 are only a few examples of the material A specimens. Figs 5 and 6 show optical microscope photographs of the material B samples. The growth and nucleation surfaces of a diamond beam sample are compared in Fig. 5, while the entry and exit surfaces of a via hole are compared in Fig. 6.

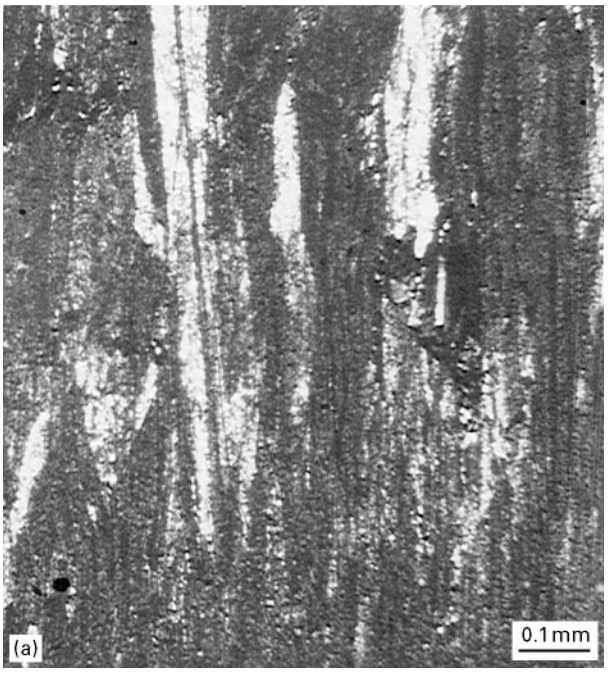

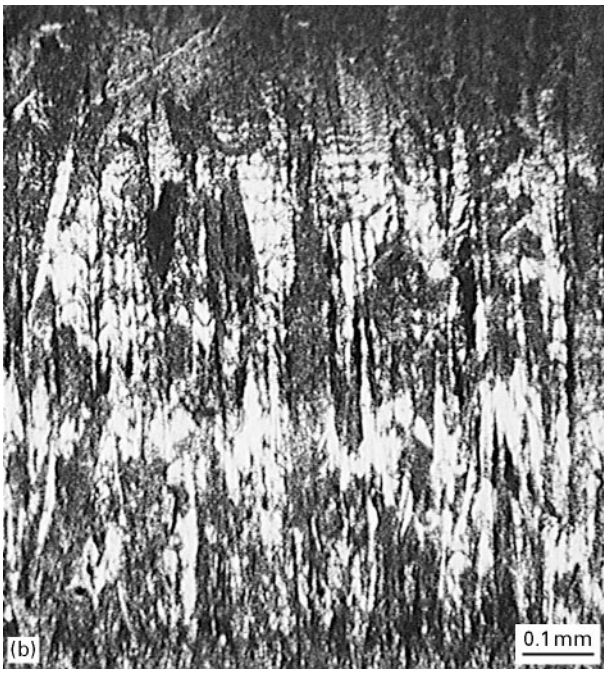

Figure 2 Side views of (a) material A and (b) material B thin diamond beams showing vertical polycrystal grains; the growth surface is along the top edge while the nucleation surface is along the bottom.

There are clear material differences between the A and B samples as contrasted in Figs 3 and 5, particularly with respect to surface characteristics. The growth surfaces of material B specimens are less rough and exhibit patterns, apparently, of similarly orientated grains. Comparing high magnification views of the growth surfaces, as seen in Figs 4a and 6b, material B does not seem to exhibit the significant crack network seen in material A. Cracks are likely present on a much finer scale in material B samples.

The laser drilled via holes also differed between the two materials. Comparing Figs 4 and 6, it can be seen that the material A holes are fairly uniform from entry to exit, while the material B holes are not. The

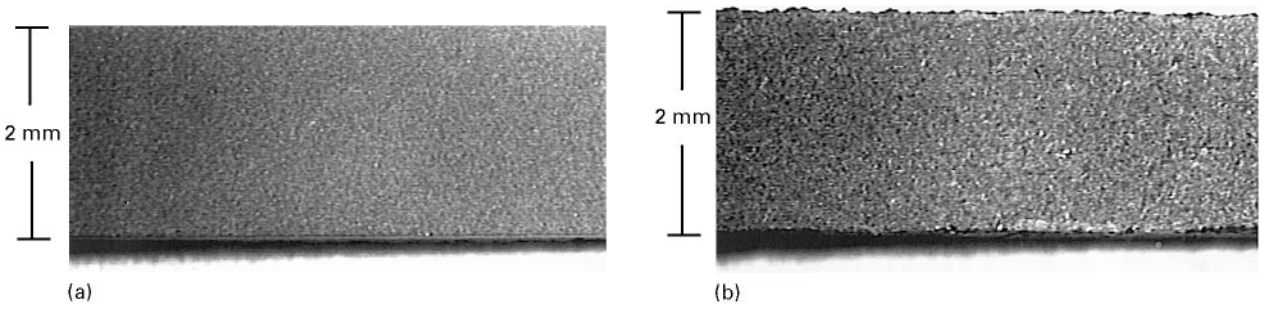

Figure 3 Nucleation surface and (b) growth surface of a material A diamond beam specimen showing differences in polycrystal grain size.

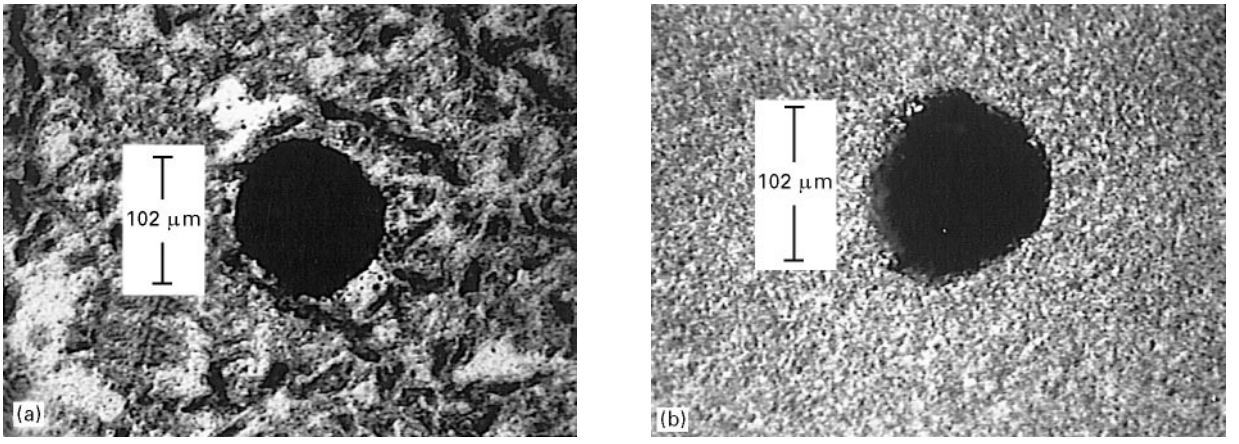

Figure 4 A laser drilled via hole in a material A diamond beam specimen, as seen from both (a) entry (growth surface) and (b) exit (nucleation surface).

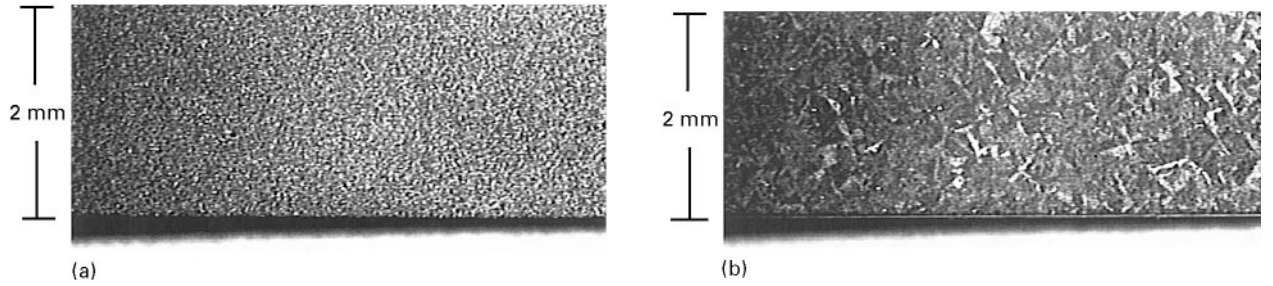

Figure 5 (a) Nucleation surface and (b) growth surface of a material B diamond beam specimen.

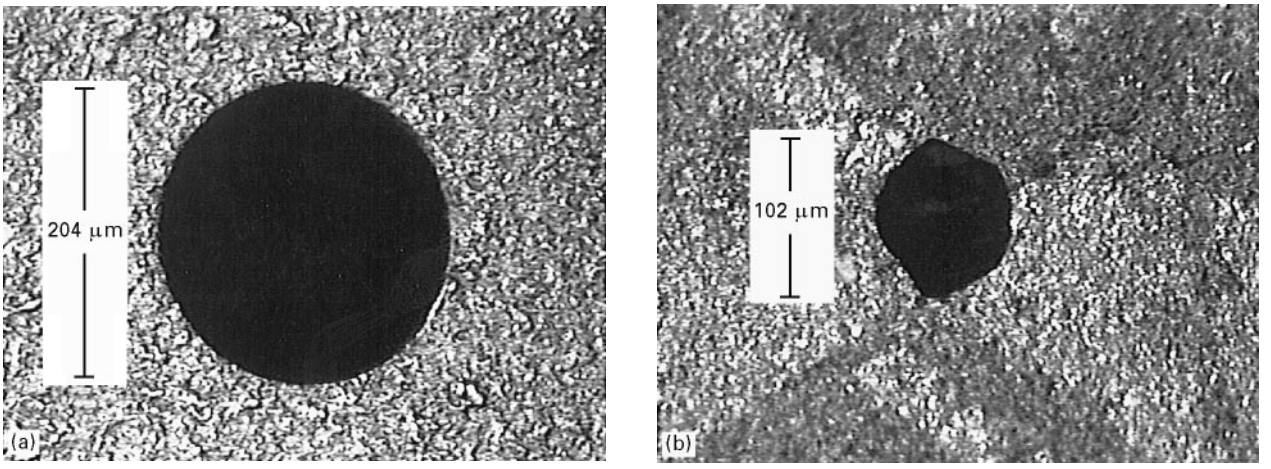

Figure 6 A laser drilled via hole in a material B diamond beam specimen, as seen from both (a) entry (nucleation surface) and (b) exit (growth surface).

diameters of the material A holes are nearly 102 μm through the thickness of the plate. The material B holes, however, are approximately 204 μm in diameter at entry and taper to approximately 102 μm at the exit surface.

Acoustic microscopy was used to survey the material volumes and to examine the sample via holes more closely. A SonoScan acoustic microscope at a frequency of 100 MHz was employed. The primary purpose of the scans was to look for evidence of radial cracking from the perimeter of the holes, not only on the surfaces of the samples but through the thicknesses as well. The via holes appeared to be very cleanly drilled and no evidence of radial cracking was found, from either the optical or acoustic microscopy studies.

2.2. Mechanical tests

2.2.1. Indentation hardness testing

Several material A samples were subjected to indenter loading with a steel ball indenter on a Rockwell test machine, as schematically illustrated in Fig. 7a. Two different ball sizes were used, specifically 1.588 and 3.175 mm diameter steel balls. Initially it was thought that the diamond material might be so brittle that ring-type or cone cracking might occur during elastic deformation of the diamond and steel ball indentation system. Hertzian elastic contact theory predicts a power law relationship between the applied load to the indenter and the surface contact area under elastic loading. The load–contact area relationship can be converted into an effective stress–strain curve. For a ball indentation test, the strain is measured as the ratio of the contact diameter, d, and the ball diameter, D, while the hardness stress, σ_H, is taken as the applied load, P, divided by the contact area, $\pi d^2/4$, thus giving the relationship [3] between stress and strain obtained from Hertzian contact theory as

$$\sigma_H = (4/3\pi)[(1-\nu_b^2)/E_b + (1-\nu_s^2)/E_s]^{-1}(d/D) \quad (1)$$

where E_b, E_s, ν_b, ν_s are the Young's moduli and Poisson's ratios for the ball and specimen, respectively. Also, the theory of indentation fracture mechanics predicts for elastic loading of very brittle materials that circular ring-type or cone cracking will occur around the edge of the contact area at a critical stress value [4], specified by the following equation

$$\sigma_c \geqslant [4E_s\gamma/\pi(1-\nu_s^2)(K_1^2+K_2^2)]^{1/2}d^{-1/2} \quad (2)$$

where γ is the crack surface energy and $(K_1^2+K_2^2)$ are dimensionless normal and shear stress intensity factors. To relate to Equation 1, the indenter ball diameter, D, can be introduced into Equation 2 to give the critical stress for cracking as a function of the square root of the indentation strain, thus yielding

$$\sigma_c \geqslant [4E_s\gamma/\pi D(1-\nu_s^2)(K_1^2+K_2^2)]^{1/2}(d/D)^{-1/2} \quad (3)$$

On an effective stress–strain basis, Equation 3 shows that σ_c is lower at larger D values [3].

A series of tests at increasing load values showed that plastic deformation of the steel ball occurred before cracking of the diamond material could be detected. However, at sufficiently large loads, segmented ring-cracking was detected in a number of cases. The faint outline of such a segmented ring-crack can be seen in Fig. 7b. Further optical examination indicated that the cracking extended from the irregular edges of the filamentary crack structure.

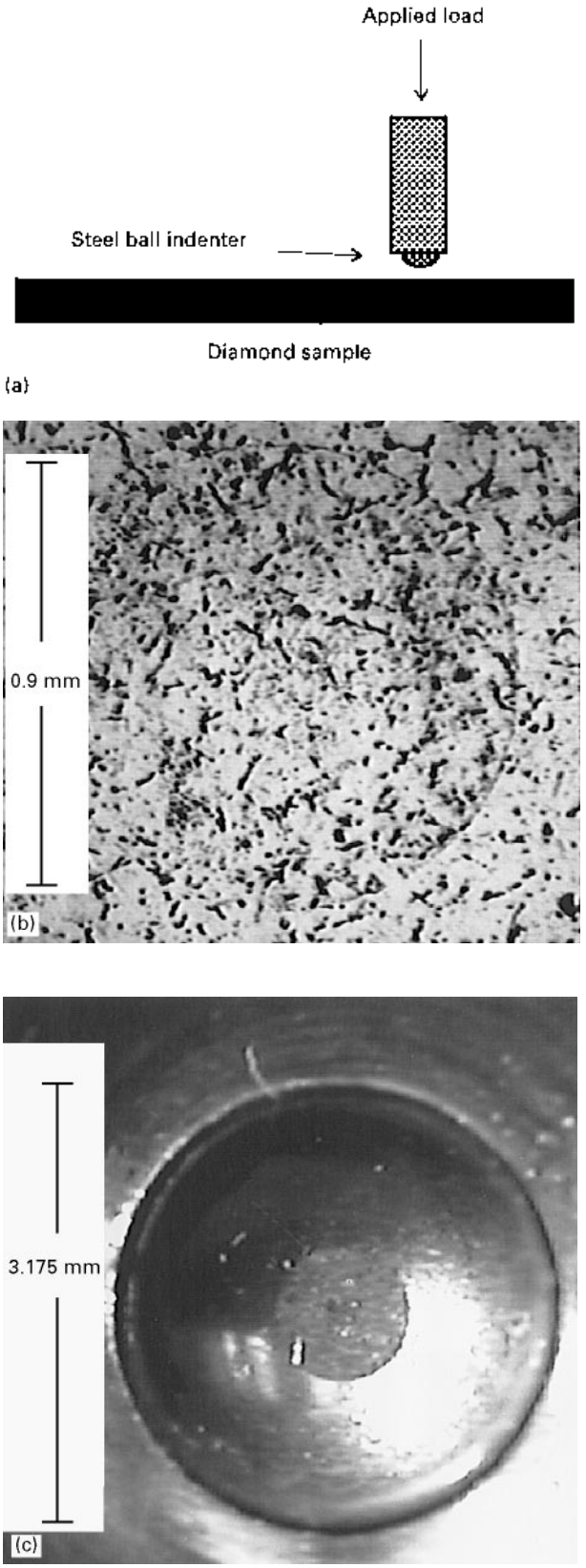

Figure 7 (a) Illustration of indentation hardness testing procedure. (b) Circular ring-type crack formed in a diamond sample, and (c) head on view of a flattened steel ball indenter.

Cathodoluminescence observations highlighted the contact areas when cracking occurred. A view of one of the "flattened" ball indenters is shown in Fig. 7c. Interferometric measurements were made on the unloaded ball surface to obtain a larger radius of curvature associated with elastic unloading of the ball from its presumed totally flat contact shape under load.

The hardness pressures and resultant strains are shown on a combined theoretical and experimental basis in Fig. 8 for various indentations made with the two ball sizes. The solid black line is the theoretical relation from Equation 1 with $E_s = 114.1 \times 10^4$ MPa, $E_b = 20.4 \times 10^4$ MPa, $\nu_s = 0.07$ and $\nu_b = 0.28$. Also shown as dotted and dashed lines intersecting the Hertzian elastic curve are the minimum critical stresses, σ_c, values predicted from Equation 3 for the onset of brittle Hertzian ring cracks, taking $\gamma = 5.3\ \mathrm{J\,m^{-2}}$ from [5] and $(K_1^2 + K_2^2) = 2.5 \times 10^{-5}$ from [4]. First consider the large strain measurements (square and circle points shown to the right of the Hertzian elastic curve) for the plastic deformation of the flattened steel balls. The residual d values were employed to compute the hardness stresses at each load value and, in turn, to determine an effective combined strain value by addition of the assumed elastic strain from the Hertzian curve and the "measured strain" from the residual d value [3]. As mentioned earlier, the larger plastic contact surface radius of curvature, that relates to the true D value for elastic unloading, gave strain values consistent with the elastic loading line in Fig. 8. From this description, then, the elastic stresses experienced by the diamond material are shown as the open square and circle points along the Hertzian elastic line.

The experimental square and circle hardness values all lie below the theoretical cracking stresses predicted for both ball diameters by Equation 3. The reason, presumably, is because of the microcracks and fissures that are present in the material. The hardness stress values for the 1.588 mm ball indenter came fairly close to the theoretical cracking stress. Beyond the consideration of higher stresses being reached at the same load values for smaller ball diameters, there is the consideration too that a smaller surface area with fewer crack nuclei are sampled with the smaller ball.

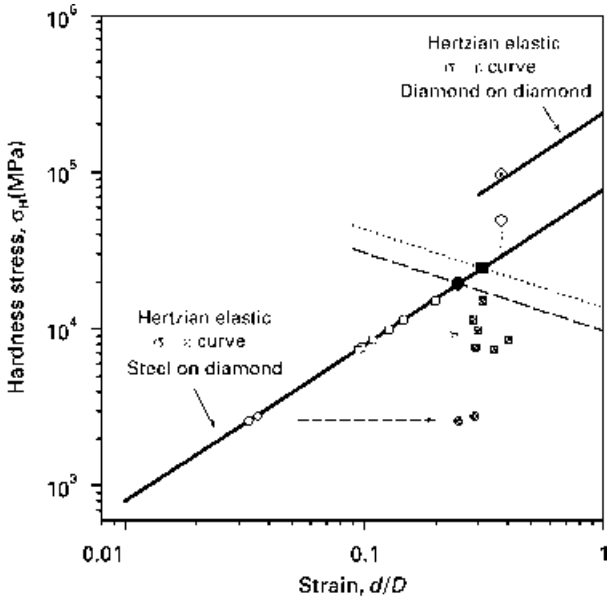

Figure 8 Hardness results for diamond on a stress–strain basis. A Hertzian elastic stress–strain curve (——) is shown along with minimum stresses to initiate ring cracking. Actual indentation data points are shown for two different indenter sizes. For $D = 3.175$ mm: (●) σ_c, (○) diamond data, (⊜) steel ball data. For $D = 1.588$ mm: (■) σ_c, (□) diamond data, (▦) steel ball data. For vickers indenter: (◆) diamond reference point, (◇) diamond data point.

In addition to the steel ball indentation tests, microindentations were attempted with a diamond pyramid tester (Vickers), leading to the detection of one residual indentation. The resulting datum point (shown as an open shaped diamond) is shown in Fig. 8 at the effective value of $(d/D) = 0.375$ that applies for this indenter shape [3]. Also shown in the figure are a reference hardness value for crack-free diamond and the (bold) Hertzian elastic line for diamond on diamond from Equation 1. The observation of the reference hardness value falling on the theoretical elastic loading line is probably coincidental. Otherwise, it should be pointed out that all of the hardness measurements shown in Fig. 8 are relatively high values, as might naturally be associated with the substantial deformation experienced by the hardened steel indenter balls.

2.2.2. Three-point bend testing

Diamond samples to be used for three-point bend tests were laser cut from the 1.0 mm thick diamond plates. The samples measured 2 mm wide by 28 mm long and were prepared both with and without laser drilled vias. The via holes were laser drilled, five in a row (lengthwise), through selected samples with either of two hole spacings: 20 or 40 mils (1 mil = 25.4 μm). In the actual design of the multichip module, the diamond substrate contains via holes at both of these spacings. The 1.0 mm plate thickness determined the beam dimensions for a reliable three-point bend test. For some material A specimens, side surfaces were polished and edges were bevelled to determine whether additional stress raisers might have been produced during specimen preparation.

The three-point bend test is schematically illustrated in Fig. 9a for experiments performed with a compression load cell on an Instron testing machine. Tests were performed with either the beam nucleation or growth side under tension for comparison, and additionally with and without laser drilled via holes. The force–displacement curves were autographically recorded by monitoring the machine crosshead velocity at a slowest rate of 0.5 mm min^{-1} and chart speed of 500 mm min^{-1}, thus providing a displacement scale of 10.0 μm corresponding to a chart length of 1.0 cm.

Fig. 10 shows comparative tensile growth surface and nucleation surface deformation curves for material A specimens obtained over a force scale of 98.1 N, giving a load increment of 5.0 N for a chart length of 1.0 cm. An essentially linear elastic force–displacement curve, including the machine deflection, was obtained. A load ratio of nearly 2 : 1 favours the greater fracture strengths sustained by the specimens with their nucleation surfaces in tension.

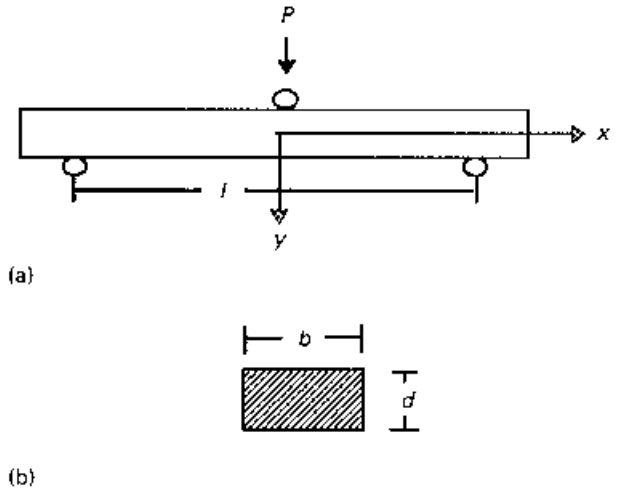

Figure 9 (a) Beam under three-point bend test, and (b) cross-sectional beam view.

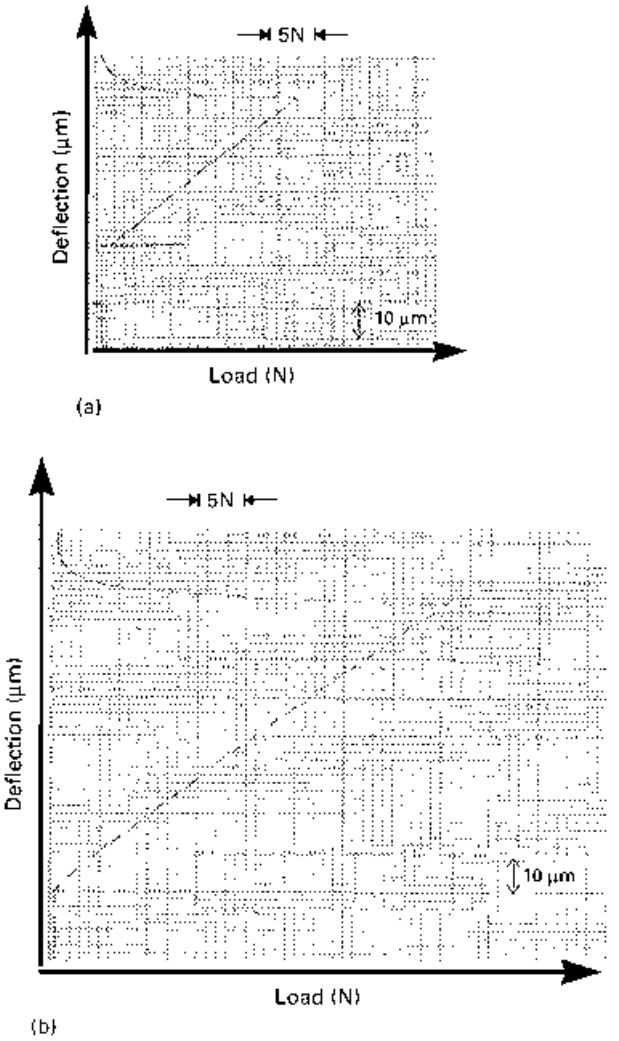

Figure 10 Typical comparison of bend test data for material A diamond: (a) growth surface under tension versus (b) nucleation surface under tension; specimen 607701.

2.2.2.1. Fracture strength measurement. The maximum fibre stress, σ_{max}, in a beam of rectangular cross-section under three-point bending occurs at the centre of the beam on the bottom surface and is approximated from elementary beam theory [6] as

$$\sigma_{max} = (M/I)y_{max} \quad (4)$$

where M is the bending moment at the middle cross-section of the beam and I is the moment of inertia (see Fig. 9). With $M = Pl/4$ and $I = bd^3/12$, then

$$\sigma_{max} = 3Pl/2bd^2 \quad (5)$$

where, for our specific test, $l = 22.86$ mm, $d = 1$ mm and $b = 2$ mm [6].

Fracture stress values were determined for each of the samples subjected to bend testing, based on the maximum load measurements, and the results are shown in Table I. The beam samples are divided into seven categories (rows) based on material A or B conditions, side edge polishing, the presence of via holes and their spacing, where applicable. For each category, four beams were tested; two with the nucleation side under tension and two with the growth side under tension. The material A samples included some beams with polished sides, as noted, because of the concern that the sharper laser cut sides might contain local stress raisers.

The most significant fracture stress comparison in Table I is between nucleation and growth surfaces. In each of the seven material categories, the fracture strength of the nucleation surface is significantly higher than the fracture strength of the growth surface. The difference is greatest for beams without via holes, where the ratio of nucleation to growth surface strength is nearly 2 : 1 for both A and B materials. For samples with via holes, the nucleation–growth surface fracture strength ratios are smaller. The bevelled edges and polished sides of selected material A specimens did not noticeably affect the fracture strength measurements.

A comparison of results between A and B materials illustrates the higher fracture strength values for the material B samples, both on the nucleation and growth surfaces. For samples without via holes the B material exhibited a fracture strength close to 1000 MPa on the nucleation surface, while the A material showed a nucleation surface fracture strength of only 700 MPa. The growth surface fracture strength comparison gave fracture strengths of 450 and 350 MPa, respectively. The same trend applies for specimens with via holes.

The via holes are seen to affect the fracture strength more on the nucleation surfaces of specimens. For material A, there is a significant decrease in nucleation surface fracture strength from roughly 700 to 500 MPa as we move from the samples without via holes to the samples with via holes at the two different spacings. The via hole effect on the material A growth surfaces is very small in comparison. An even more significant via hole effect is observed in material B, where the nucleation surface fracture strength decreases from 950 MPa without holes to 600 MPa with holes. This is almost as significant as the decrease observed when comparing the nucleation/growth surfaces of the material B samples without holes, where the fracture strengths decreased from 950 to 450 MPa. On material B growth surfaces, a very small via hole effect is again observed.

TABLE I Maximum stress values for material A and B diamond beam samples subjected to three point bending (results are grouped by material categories)

Material conditions	Nucleation side under tension		Growth side under tension	
	Sample No.	σ_{max} (MPa)	Sample No.	σ_{max} (MPa)
1. Material A, no holes, polished sides	607702-1	647.8	607702-3	277.6
	607702-2	673.0	607702-4	265.9
2. Material A, no holes, unpolished sides	607701-1	684.8	607701-3	370.2
	607701-2	777.4	607701-4	304.5
3. Material A, with holes, 40 mil separation	607703-1	504.8	607703-3	329.8
	607703-2	504.8	607703-4	311.3
4. Material A, with holes 20 mil separation	607704-1	511.5	607704-3	260.8
	607704-2	462.7	607704-4	269.2
5. Material B, no holes	dnh-1	950.7	dnh-3	506.5
	dnh-2	984.3	dnh-4	440.8
6. Material B, with holes, 40 mil separation	d40-1	588.9	d40-3	445.9
	d40-2	619.2	d40-4	489.6
7. Material B, with holes, 20 mil separation	d20-1	605.7	d20-2	454.3
	d20-3	620.9	d20-4	390.4

2.2.2.2. Elastic constant estimates. The slow beam loading (at 0.5 mm min^{-1}) and maximum chart speed recording (at 500 mm min^{-1}) allowed enough of a chart record to be obtained to estimate the Young's modulus of the diamond plates, after determination of the spring constant for the testing machine and beam test fixture. Again, from elementary beam theory [6] the relevant expression for the maximum centre deflection, y_c, of the beam is

$$y_c = Pl^3/4Ebd^3 \quad (6)$$

where E is the Young's modulus of the beam. By substitution of σ_{max} from Equation 4, then

$$E = (\sigma_{max}/y_c)(l^2/6d) \quad (7)$$

When determining the beam deflection from the chart data, as mentioned, the machine deflection needs to be subtracted from the total deflection. The procedure involved superposing data curves and subtracting values, and as such naturally introduced additional experimental error. Alternatively, E was estimated, using Equation 6, from the slope of the linear loading dependence predicted for P versus y_c as

$$E = (l^3/4bd^3)(\Delta P/\Delta y_c) \quad (8)$$

again, involving subtraction of the machine deflection from the recorded load–deflection curve. The roughly estimated E values are listed in Table II with the experimental measurements employed for the calculations.

TABLE II Young's modulus data from three-point bend tests

Sample	y_c (μm)	P (N)	σ_{max} (MPa)	E ($\times 10^6$ MPa)
607702-1	52	37.8	647.8	1.085
607702-2	54	39.2	673.0	1.086
607702-3	20	16.2	277.6	1.209
607702-4	23	15.5	265.9	1.007
607701-1	50	40.0	684.8	1.193
607701-2	60	45.3	777.4	1.128
607701-3	26	21.6	370.2	1.240
607701-4	25	17.8	304.6	1.061
607703-1	36	29.4	504.8	1.221
607703-2	38	29.4	504.8	1.157
607703-3	27	19.2	329.8	1.064
607703-4	23	18.1	311.3	1.179
607704-1	40	29.8	511.5	1.114
607704-2	40	27.0	462.7	1.008
607704-3	22	15.2	260.8	1.033
607704-4	23	15.7	269.2	1.019
dnh-1	60	55.4	950.7	1.380
dnh-2	56	57.4	984.3	1.531
dnh-3	33	29.5	506.5	1.337
dnh-4	28	25.7	440.8	1.371
d40-1	39	34.3	588.9	1.315
d40-2	40	36.1	619.2	1.348
d40-3	32	26.0	445.9	1.214
d40-4	36	28.5	489.6	1.185
d20-1	40	35.3	605.7	1.319
d20-2	31	26.5	454.3	1.276
d20-3	46	36.2	620.9	1.176
d20-4	27	22.8	390.4	1.259

Fig. 11 displays the Young's modulus estimates for the various material conditions with material A estimates shown in black and white and material B estimates shown as shaded and white. Empty and filled circles delineate which surface was under tension. An effective average Young's modulus reference value of 1.141×10^3 GPa from single crystal compliance data [5] is shown as the straight line constant value for comparison. The relative differences in E values between the two materials appears to be significant.

The fact that the estimated E values are quite close to the averaged reference value is encouraging. The E values for material B are noticeably higher than the E values for material A, particularly for the samples without via holes. One might expect the estimated Young's modulus to be less than the averaged Young's modulus obtained from single crystal diamond because of the internal crack structure and fissures present within the polycrystalline material, although such cracks and fissures are noticeably absent in the B material. The higher E value estimates for material B may reflect the fact that the material has a

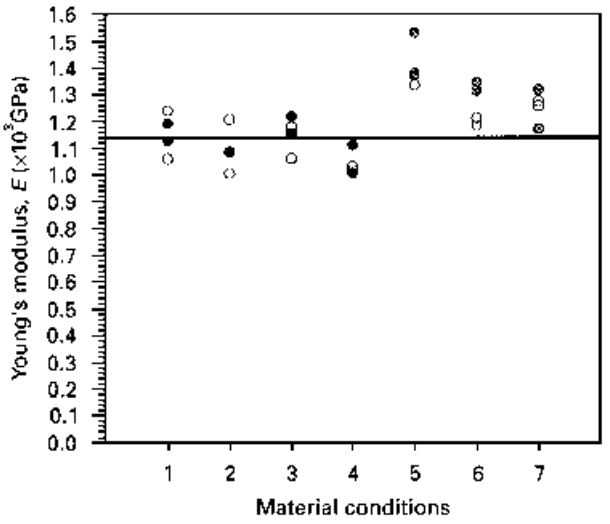

Figure 11 Young's modulus estimates for material A and B diamond beam specimens, shown for various material categories (refer to Table I). For material A: (●) nucleated side under tension, (○) growth side under tension. For material B: (◍) nucleated side under tension, (○) growth side under tension.

crystallographic texture as indicated in Fig. 6. On this basis, an estimate has been made of a 20% increase in the E value to be expected for grains aligned with their crystal axes along the $\langle 1\,1\,1 \rangle$ direction through the plate thickness. This is the expected growth direction for the diamond plates.

2.2.2.3. ANSYS model description.* The three-point bend tests were modelled with the ANSYS finite element software package. Widely used in the computer-aided engineering field, ANSYS performs structural analyses on solid models and can be used to study the physical responses of a model under loading. Constructing a solid model of the bend test and applying similar loads as in the laboratory, the ANSYS computed stresses and deflections were in close agreement with the experimental measurements. For example, the three-dimensional model of the diamond beam samples, with $E = 1.141 \times 10^3$ GPa and ν = Poisson's ratio = 0.07, is shown in Fig. 12 loaded with a point load force of 40 N to simulate the stress state in an actual bend test. A contour plot of the resultant stress in the x-direction, S_x, is shown in Fig. 12a. The S_x values range from a compressive stress of 682 MPa at the load application, to a tensile stress of 673 MPa on the tensile surface of the beam. Referring to Table I, this tensile stress is in close agreement with the nucleation surface bend test for material A without via holes. A magnified view of the stress distribution near the application of the load is shown in Fig. 12b. The green band in the middle is where the stress is essentially zero. The magnified view indicates that the very highest stress values are limited to a narrow band near the tensile surface and do not penetrate very far into the

*ANSYS is a registered trademark of ANSYS, Inc., formerly Swanson Analysis Systems, Inc.

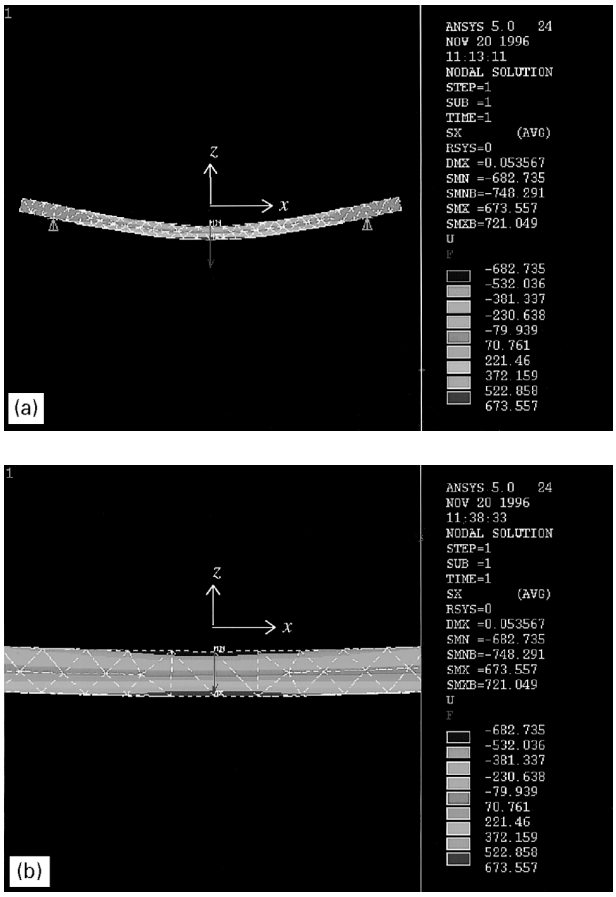

Figure 12 ANSYS modelling results detailing (a) the resultant stress distribution for the bend test model and (b) a magnified view of the stress distribution near the maximum load point.

thickness of the beam. One contour width from the tensile surface the stress has already decreased from 673 to 522 MPa. On a linear elastic basis, one should expect a stress of 522 MPa at a distance of 0.11 mm above the tensile surface.

While a view of the vertical deflection, U_z, is not shown, maximum deflection occurs in the centre of the beam, directly under the load, and measures 53 μm. Referring to Table II, this deflection is comparable to the deflections measured for material A samples without via holes, when the nucleated side is under tension.

3. Discussion

3.1. Profilometry, SEM fractography and fracture surface topography analysis (FRASTA)

The three-point bend test fractured specimens were studied in detail to gain information about the microstructural and via hole connections with the material mechanisms. SEM observations were made by placing the broken beam halves together with their tensile surface edges in contact, as shown in Fig. 13, for the beam fracture surfaces to be seen in a "folded open" view. Measurement of the fracture surface elevations either along a line trace or, more completely, on an area basis provides a method of measuring the sequential separation stages of the fracturing process. The

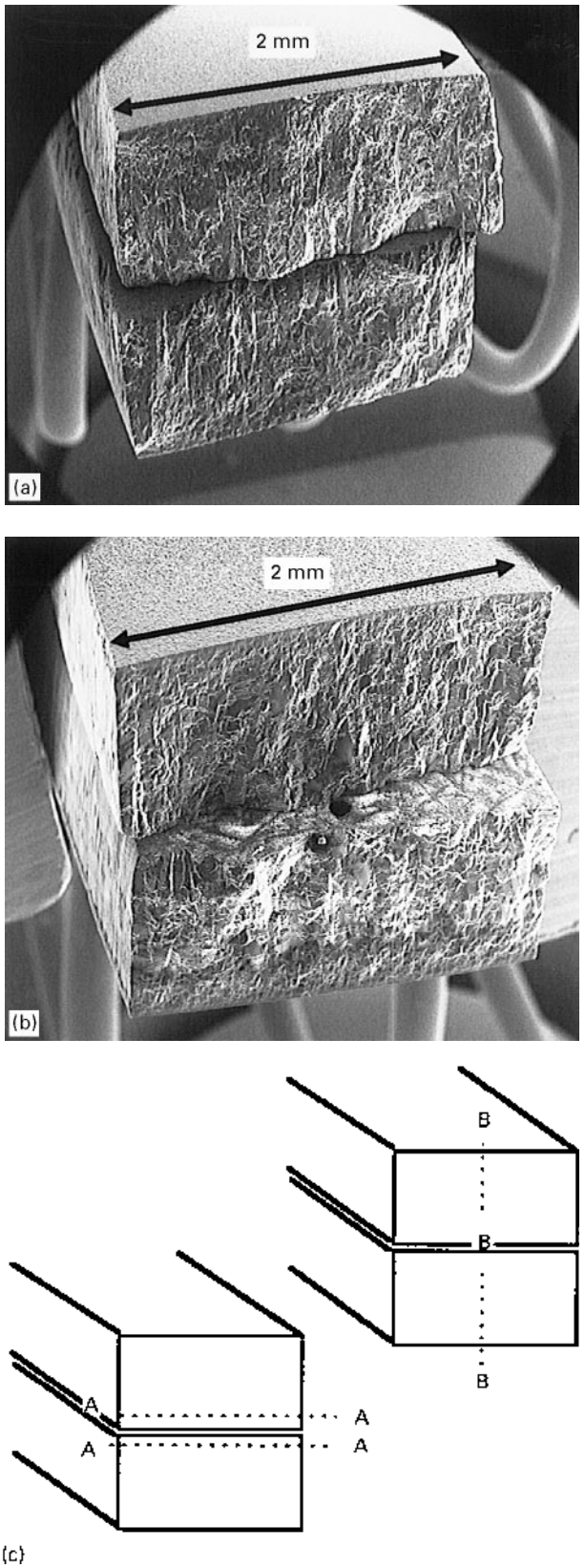

Figure 13 SEM photographs showing the fracture surfaces from (a) material A and (b) material B beam samples that were analysed via FRASTA. (c) Contour paths A–A and B–B for FRASTA results are also shown for later reference.

otherwise matching surface profiles are brought together in juxtaposed matching orientations to show, at first contact, the last fractured ligament between the specimen halves and, at last points to touch, the first origins of the fracturing process [7].

Initial SEM photographs showed topographical differences between average fracture surface qualities of material A and B specimens. The fracture surfaces of material A specimens were relatively rough while the material B fracture surfaces were relatively flat. In addition, observations of the material B fracture surfaces, along the growth surface edge where cracking initiated, revealed linear segments suggestive of cleavage along $\{1\,1\,1\}$ planes. These observations led to a more detailed study of the fracture surfaces using the newer method of fracture surface topography analysis, FRASTA [8, 9].

Fig. 13 shows representative SEM results for broken samples from material A and B tests with the growth side under tension in each case. Also shown in the figure, for later reference, are horizontal and vertical contour paths along which FRASTA results were obtained.

The FRASTA method combines a confocal-optics-based scanning laser microscope and attached computer software, to match the three-dimensional features of conjugate fracture surfaces and to reconstruct the detailed fracturing sequence [8]. The FRASTA results are viewed in one way by a series of cross-sectional plots (XSPs) showing views perpendicular to the fracture surface that reveal the matching of conjugate surfaces and also display the existence of microcracks [8, 9].

Representative XSPs from the two beam samples of Fig. 13 are shown in Figs 14 and 15. For each sample, both a horizontal and vertical XSP are displayed along the contour lines previously noted in Fig. 13. The topographical map displacements for the XSPs are also given for both samples, at a point where the fractured area measured roughly 30–35% of the total area. In these XSPs, the white areas represent regions where the conjugate topographs do not overlap, and signify cracks or voids associated with the opening fracture faces. Dark regions are those where the two specimen halves overlap and indicate the extent of plastic deformation before fracture.

Figs 14 and 15 illustrate the main conclusions that were drawn from the FRASTA analysis. As mentioned from the SEM observations, the fracture surfaces of material A appeared rougher than for material B. The FRASTA XSPs in Fig. 14 confirm the observation. The material A surface profile (Fig. 14a) is observed to be rough and wavy while the material B surface profile (Fig. 14b) is flatter (though on a slight incline). The earlier mentioned optical microscope observations of filamentary surface cracks in material A, combined with these FRASTA plots, lead to the conclusion that material A actually fractures along the incipient crack networks and hence produces the wavy or rough surface profiles. The observation is unusual in that a rougher fracture surface for a ductile material is normally associated with a higher fracture strength. Material B, with fewer surface cracks, fractures in a more planar manner revealing a flatter surface profile.

Also observed in the plots of Fig. 14 are the presence of large vertical slits (white spikes) intersecting the main fracture surfaces of material B; such slits are

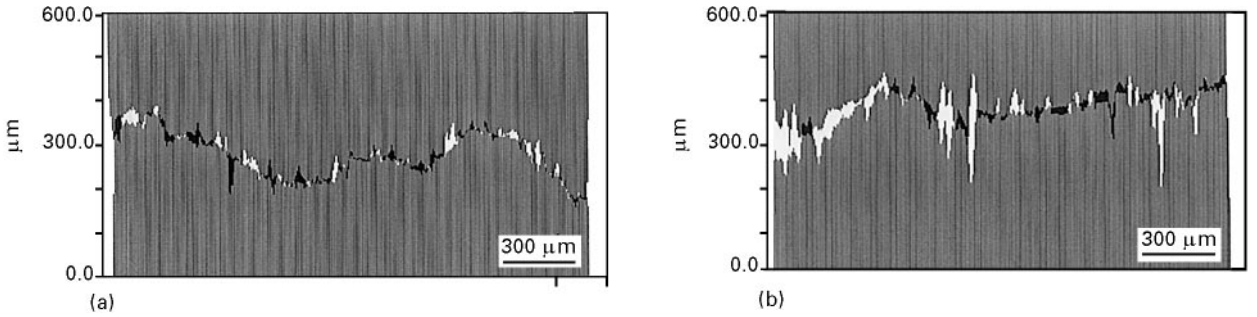

Figure 14 FRASTA results showing horizontal cross-sectional plots (XSPs) for material A and B broken beam samples along contour paths shown previously in Fig. 13. (a) Material A specimen, XSP along the A–A, map displacement = 310.6 μm. (b) Material B specimen, XSP along line A–A, map displacement = 406.6 μm.

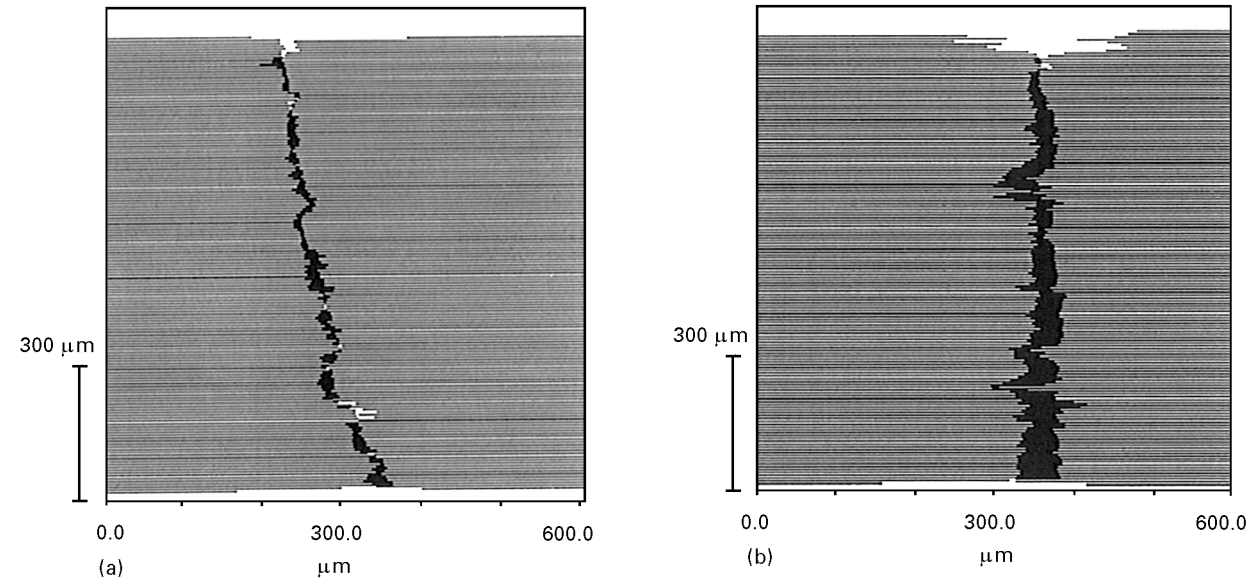

Figure 15 FRASTA results showing vertical cross-sectional plots (XSPs) for material A and B broken beam samples along contour paths shown previously in Fig. 13. (a) Material A specimen, XSP along the B–B, map displacement = 310.6 μm. (b) Material B specimen, XSP along line B–B, map displacement = 406.6 μm.

absent in material A. The long slits suggest that material B undergoes a different fracturing mechanism apparently consistent with the observation of planar cleavage-like traces possibly produced by $\{1\,1\,1\}$ crystallographic planes in material B, again consistent with earlier mentioned observations of flat planar crack surface elements in the SEM photographs.

The Fig. 15 XSPs that span the through-thickness dimension of the beams reveal surprising evidence of wedge-like opening in the material B specimens. This is seen by the increase in width of the fracture surface separation when traversing from the compression to the tensile surface (top) where cracking initiated. The smoothly increasing region of overlap suggests that material B specimens underwent plastic deformation as part of the overall fracturing process [10]. Material A does not exhibit this same region of overlap and the corresponding topographical maps could be matched up with a negligible tilt. Quantitative measurements, from Fig. 15, of the overlap region in material B may be an overestimate as the tilting of the specimen halves exaggerates the darkened areas [10]. However, it is clear that material B has a wider region of overlap suggesting plastic deformation. Such plastic deformation adds to the reasonableness of the higher fracture strengths being measured for material B specimens.

4. Conclusions

A reasonable understanding has been generated of quantitative strength measurements obtained for two industrial diamond materials, with and without laser drilled holes employed for electronic application. Optical, acoustic and scanning electron microscopy observations have revealed distinct features of growth and nucleation surface structures in the two materials as well as to the quality of laser drilled via holes in the diamond plates, relating to indentation cracking and fracture strength measurements. The FRASTA method of analysis provided particularly useful information on the cracking behaviour of each of the two materials studied, especially connecting with a rougher crack-joining path for the failure of material A specimens and cleavage-like behaviour in the stronger B material. Somewhat surprising evidence was obtained for plastic deformation having occurred in the fracturing of material B specimens.

Acknowledgements

The authors would like to express their appreciation to the many individuals who contributed to this study. Jim Butler and Dan Vestyck (Naval Research Laboratory) assisted with the laser cutting of diamond beams as well as the laser drilling of via holes performed on diamond scrap samples in the early stages of the analysis. They also performed the cutting of the beam samples from the broken diamond substrate. Nick Strifas (University of Maryland) performed the acoustic microscopy measurements and produced the photos that were used to examine the via holes. X. J. Zhang (University of Maryland) assisted with the hardness indentation tests. John Fitz (Laboratory for Physical Sciences) provided much help and training with the scanning electron microscope. Both Albert Leyendecker and John Fitz (Laboratory for Physical Sciences) were involved with and gave critical guidance concerning cathodoluminescense studies. Dave Evans and Scott Merritt (University of Maryland) assisted with initial profilometry measurements as well as several interferometry calculations. Takao Kobayashi (SRI International) conducted an extensive analysis of the fracture surfaces of several broken beam samples, using FRASTA techniques. Warren Beard (Laboratory for Physical Sciences) gave additional assistance with the optical microscopy.

References

1. P. J. BOUDREAUX, in "Applications of diamond films and related materials: Third international conference", Gaithersburg, August 1995, edited by A. Feldman, Y. Tzeng, W. A. Yarbrough, M. Yoshikawa and M. Murakawa (NIST SP 885, Gaithersburg, MD, 1995) p. 603.
2. P. J. BOUDREAUX and C. CULHANE, "Synthetic diamond: a hard rock story that moved supercomputing out of the basement", Laboratory for Physical Sciences, College Park, MD, internal technical report (1996).
3. B. L. HAMMOND and R. W. ARMSTRONG, *Phil. Mag. Lett.* **57** (1988) 41.
4. B. R. LAWN, *J. Appl. Phys.* **39** (1968) 4828.
5. J. E. FIELD, in "Properties and growth of diamond" edited by G. Davies (INSPEC, The Institution of Electrical Engineers, London, 1994) p. 36.
6. C. CM. WU, Private communication.
7. K. OGAWA, X.-J. ZHANG, T. KOBAYASHI, R. W. ARMSTRONG and G. R. IRWIN, in "Microstructural aspects of the fracture toughness cleavage–fibrous transition for reactor-grade steel", Fifteenth National Symposium on Fracture Mechanics, College Park, July 1984, edited by R. J. Sanford (ASTM STP 833, Philadelphia, PA, 1984) p. 393.
8. T. KOBAYASHI and D. A. SHOCKEY, *Adv. Mater. Processes* **140** (1991) 28.
9. *Idem*, *ibid.* **140** (1991) 24.
10. T. KOBAYASHI, Private communication.

Received 14 March
and accepted 25 March 1997